International Journal of Nanomedicine

Dovepress
Taylor & Francis Group

Open Access Full Text Article

ORIGINAL RESEARCH

In vivo Targeted Delivery of Extracellular Vesicle–Gold Nanorod Hybrids to Metastatic Melanoma Lung Tumors

Karen Bolaños[1–3], Daniela León[1–3], Pedro Jara-Guajardo[2,3], Pamela Contreras[1], David Silva Ancahuail[3], Ana Luisa Riveros[2,3], Yanay Montano[2,3], Damián Pérez[2,3], Eyleen Araya[4], Marcelo J Kogan[2,3], Andrew FG Quest[1,3]

[1]Laboratory of Cellular Communication, Center for Studies on Exercise, Metabolism and Cancer (CEMC), Program of Cell and Molecular Biology, Faculty of Medicine, Institute of Biomedical Sciences (ICBM), University of Chile, Santiago, Chile; [2]Departamento de Quimica Farmacologica y Toxicologica, Facultad de Ciencias Quimicas y Farmaceuticas, Universidad de Chile, Santiago, Chile; [3]Advanced Center for Chronic Diseases (ACCDIS), Facultad de Medicina and Facultad de Ciencias Quimicas y Farmaceuticas, Santiago, Chile; [4]Departamento de Ciencias Quimicas, Facultad de Ciencias Exactas, Universidad Andres Bello, Santiago, Chile

Correspondence: Marcelo J Kogan, Departamento de Química Farmacológica y Toxicológica, Facultad de Ciencias Químicas y Farmacéuticas, Universidad de Chile, Santiago, 8380494, Chile, Email mkogan@ciq.uchile.cl; Andrew FG Quest, Cellular Communication Laboratory, Center for Studies on Exercise, Metabolism and Cancer (CEMC), Instituto de Ciencias Biomédicas (ICBM), Facultad de Medicina, Universidad de Chile, Santiago, 8380453, Chile, Email aquest@u.uchile.cl

Background: Cutaneous melanoma is an aggressive type of cancer characterized by rapid progression, resistance to chemotherapy, and metastasis to the lung. Conventional chemotherapy and radiotherapy are the principal approaches for treating metastasizing tumors, but the lack of targeting results in severe side effects and low treatment efficacy. Nanoparticles reportedly increase selectivity, given that they can accumulate at specific locations owing to the enhanced permeation and retention (EPR) effect. In this respect, plasmonic nanoparticles, such as gold nanorods (AuNRs), are interesting because of their photothermal and optical properties, making them suitable for biomedical applications, such as drug delivery, tumor ablation, and theranostics. To increase the tumor accumulation of AuNRs, extracellular vesicles (with sizes ranging from 40–150 nm) have attracted attention because of their remarkable biocompatibility and natural cell-accumulation selectivity. To further increase the targeting properties of the nanosystem, we functionalized the AuNRs with methotrexate (MTX), which is known to interact with the overexpressed folate receptors in cancer cells. We combined the inherent homing properties of exosomes from B16F10 cells with the active targeting properties of MTX to increase the accumulation of AuNRs in metastatic lung melanoma tumors.

Methods: We obtained and exhaustively characterized B16F10 exosomes loaded with MTX-functionalized AuNRs (EXOS-AuNR-MTX). The safety of the complete nanosystem, as well as its specific and time-dependent accumulation in B16F10 cells, was determined using the mitochondrial MTS assay and fluorescence analysis, respectively.

Results: Surface functionalization with MTX in combination with B16F10 EXOS was used to promote the accumulation of AuNRs in metastatic lung nodules, with significantly greater amounts of gold in the tumors following EXOS-AuNR-MTX treatment than following only AuNR-MTX treatment, as was determined in vivo and ex vivo by quantitative gold measurements. Remarkably, 5.5% of the injected dose of the AuNRs was recovered at the tumor sites, whereas only 1% of the injected dose usually accumulated in tumors due to the EPR effect, as reported. We further confirmed the preferential accumulation of AuNRs from EXOS-AuNR-MTX rather than from AuNR-MTX in tumor vessels and tumor nodules rather than healthy tissues by histological analysis.

Conclusion: Our approach provides a valuable tool to improve the accumulation of gold nanoparticles in metastatic tumor nodules by combining the natural properties of exosomes to drive the targeting of AuNR-MTX.

Keywords: exosomes, gold nanorods, methotrexate, targeting, drug delivery, metastasis

Received: 8 January 2025
Accepted: 14 April 2025
Published: 30 May 2025

Graphical Abstract

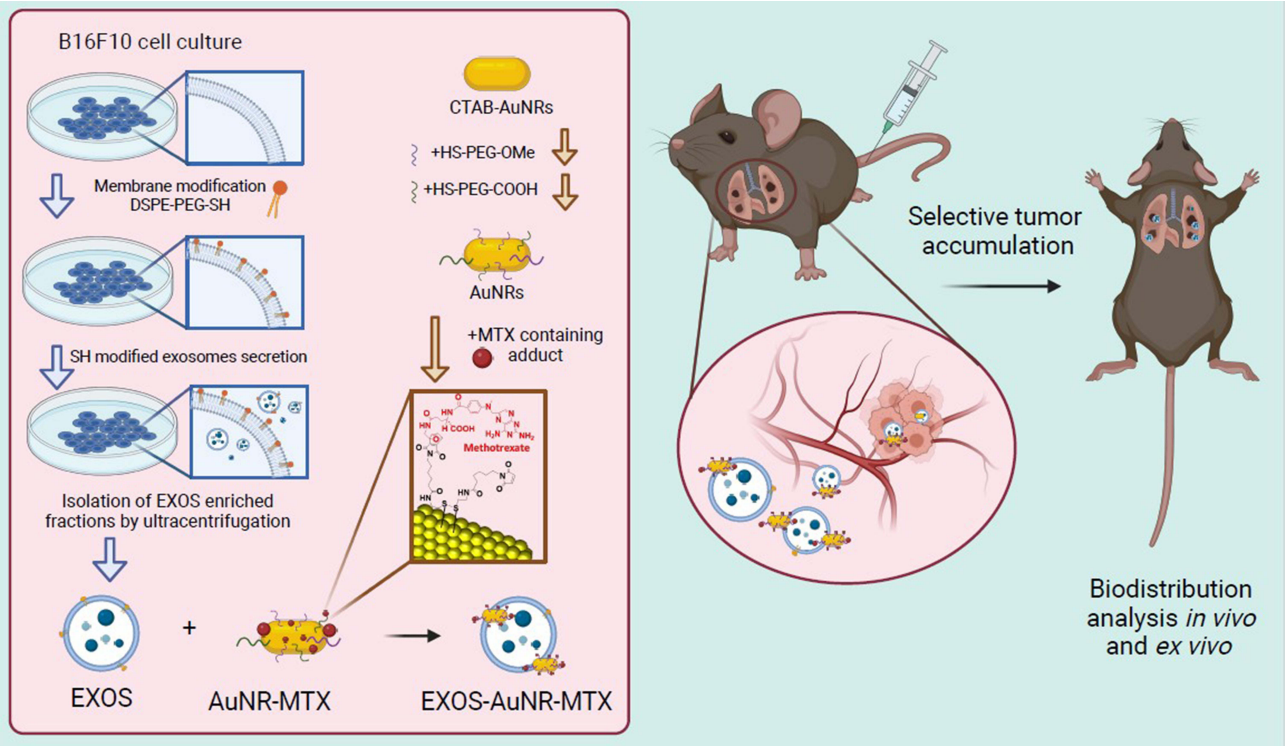

Introduction

Cancer represents a group of diseases characterized by genetic and epigenetic alterations that lead to uncontrolled cell proliferation, cell transformation and, ultimately, metastasis.[1] Among these diseases, cutaneous melanoma is one of the most aggressive types, with an increasing global incidence.[2] Its rapid progression, elevated metastatic potential, particularly to the lungs[3,4] and resistance to conventional treatments make it a major therapeutic challenge. Currently, chemotherapy and radiotherapy are the principal strategies for managing metastatic melanoma.[5] However, their lack of selectivity between cancerous and normal cells leads to severe side effects and reduced treatment efficacy, highlighting the urgent need for more targeted and effective therapeutic approaches.[6–8]

Nanoparticle (NP)-based drug delivery has emerged as a promising alternative for improving cancer therapy, given that they can accumulate in tumors via the enhanced permeation and retention effect (EPR).[9] This effect is attributable to the leaky vasculature in tumors, in combination with a dysfunctional lymphatic system that facilitates the retention of AuNPs at tumor sites.[10] As a consequence, NPs loaded with drugs are delivered to specific locations.[11,12] The use of plasmonic NPs, such as gold nanoparticles (AuNPs), represents an interesting option for temporally controlled drug release because they efficiently convert a light stimulus into heat owing to the *photothermal effect*.[13] Among the various shapes of AuNPs, gold nanorods (AuNRs) are of particular interest because of their high photothermal efficiency (approximately 30–40%)[13–20] and modulable light absorption properties, which can be manipulated by changing their axis ratio. This light absorption can be tuned to near-infrared (NIR) biological windows (first 700–980 nm and second 1000–1200 nm),[21] where biomolecules display low absorption and irradiation results in high tissue penetration.[22] For cancer treatment applications, the heat produced by AuNRs after NIR irradiation can be used for photothermally controlled drug delivery,[23] as well as tumor ablation by hyperthermia and cell death via reactive oxygen species (ROS) production.[24–28] On the other hand, AuNRs also have photoacoustic, light scattering and X-ray attenuation

properties, making them potentially useful for medical imaging applications, such as computed tomography (CT), surface-enhanced Raman spectroscopy (SERS) and magnetic resonance imaging.[28–31]

Given the broad range of biomedical applications that therapies with AuNRs can offer, it is desirable to design approaches that permit increasing the accumulation of these NPs in tumor tissues. Unfortunately, although the AuNRs can reach the tumor tissue via the passive EPR effect, this per se is inefficient, and less than 1% of the administered doses reach their target.[32,33] To overcome this limitation, surface modification of AuNRs with different ligands, including cell-penetrating peptides,[34,35] folic acid,[36,37] folic acid analogs[38–41] and proteins,[42–44] among others, has been shown to increase AuNRs internalization by cells in tumors (active targeting). In this study, we surface-functionalized AuNRs with methotrexate (MTX), an analog of folic acid (FA), with similar structural and physicochemical properties but higher affinity than FA for folic acid receptors overexpressed in cancer cells.[45–47] MTX was linked to the gold surface by a previously reported adduct,[48] consisting of an S-S-containing linker, bound to the AuNR surface via S-Au bonds, which function as spacers between the gold surface and MTX. In this manner, the pteridine rings of MTX, mainly responsible for the interaction with folate receptors,[49,50] remain exposed and available for interaction with the folic acid receptors on cancer cells (see Graphical Abstract).

Although active targeting via interaction with folate receptors that are overexpressed in cancer cells increases the uptake of AuNRs in cancer cells, it remained necessary to develop a strategy that permits protection of the AuNRs in circulation while ensuring their increased accumulation at tumor sites before their internalization by tumor cells. Interestingly, the use of extracellular vesicles (EVs) produced by cells can increase the targeting and accumulation of AuNRs at tumor sites. Moreover, extracellular vesicles (EVs), particularly exosomes, have emerged as promising natural carriers for targeted drug delivery and have been shown to increase the accumulation of AuNRs at tumor sites.[51–56] One group of EVs, exosomes, range in size from 40–150 nm,[57,58] possess a lipid bilayer and contain specific proteins, as well as the RNAs of the parental cells from which they are secreted.[59] Exosomes have attracted considerable attention because of their remarkable biocompatibility and natural homing selectivity properties. Specifically, these findings suggest that exosomes derived from a particular cell line are preferentially taken up by the same cell line.[60,61] In this study, we exploited the homing properties of exosomes from the B16F10 melanoma cell line to increase the accumulation of AuNRs at tumor sites via a previously reported strategy.[37] In brief, the phospholipid layer of the exosomes was modified with amphiphilic DSPE-PEG-SH, and then, the AuNRs were conjugated to the exosomes by the formation of Au-S bonds. This strategy was found to preserve the tumor-targeting and intrinsic functionalities of the exosomes and increase the tumor accumulation of the AuNRs.[37] Previous studies have investigated the use of exosomes and nanorods for targeting solid tumors;[37] however, their application for targeting metastatic melanoma lung tumors, which is more complex, has not yet been explored.

Therefore, in this study, we combined the homing properties of exosomes from B16F10 cells with the active targeting properties of MTX mediated by the interaction with overexpressed folate receptors in cancer cells to increase the accumulation of AuNRs in metastatic lung melanoma tumors (see Graphical Abstract). To evaluate the effectiveness of this nanosystem, we conducted in vivo biodistribution studies in a C57BL/6 mouse model of metastatic lung melanoma. This dual-targeting approach aimed to improve the selective delivery of AuNR-MTX to metastatic lung tumors, thereby addressing the limitations of both passive and active targeting strategies. To the best of our knowledge, this is the first study in which MTX-functionalized AuNRs were combined with autologous B16F10 cell-derived exosomes to achieve specific targeting of metastatic melanoma lung tumors in vivo with potential implications for enhancing the therapeutic efficacy of AuNR-based treatments in metastatic cancer.

Materials and Methods

Materials

Gold (III) chloride hydrate ($HAuCl_4$), hexadecyltrimethylammonium bromide (CTAB), silver nitrate 99% ($AgNO_3$), ascorbic acid 99% and sodium tetrahydridoborate ($NaBH_4$) were purchased from Sigma–Aldrich (St. Louis, MO, USA). Polyethylene glycol 5 kDa (SH-PEG-COOH, 5 kDa) was acquired from JenKem Technology (TX, USA). The Milli-Q water used in all the experiments was obtained via the purification of distilled water with a Simplicity SIMS 00001

(Millipore, Molsheim, France). The cell culture plates and flasks were purchased from Corning Costar (NY, USA). Penicillin/streptomycin, fetal bovine serum, the L3224 cell live/death kit, DMEM, RPMI cell culture medium, DiR (D12731, Life Technologies) and DiD (D7757, Life Technologies) were purchased from Thermo Fisher Scientific (OR, USA). DSPE-PEG-SH was purchased from Avanti (AL, USA).

Methods

Synthesis and Characterization of AuNR-CTAB

AuNRs-CTAB were synthesized via the seed-mediated procedure as previously reported.[35] Briefly, a 0.3 mm $HAuCl_4$ solution in a matrix of 0.1 M CTAB was reduced in ice-cold 10 mm $NaBH_4$ to generate the seed solution. A growth solution was prepared by reducing 0.5 mm $HAuCl_4$ solution in a 0.1 M CTAB matrix using ascorbic acid in the presence of $AgNO_3$. Subsequently, 120 µL of the seed solution were added to the growth solution and allowed to rest for 30 min at 30 °C. The obtained AuNRs-CTAB were subsequently centrifuged twice at 13000 × g for 30 min, after which the resulting pellet was resuspended in Milli-Q water.

Preparation of AuNRs and AuNRs-MTX

To 10 mL containing 1 nM of the previously obtained AuNRs-CTAB, 100 µL of a 1 M KOH solution were added to adjust the solution to pH=10. Then, 50 µL of a 1 mM HS-PEG-OMe solution were added, and the mixture was allowed to incubate for 10 min while stirring. The obtained nanoparticles were centrifuged at 13,000 × g for 10 min, and the pellet was subsequently resuspended in 10 mL of Milli-Q water. Then, 100 µL of KOH and 300 µL of a 1 mm HS-PEG-COOH solution were added. The solution was then stirred for 1 h and sonicated for another 15 min. The resulting AuNRs were centrifuged at 13,000 × g for 10 min, and the pellet was resuspended in 10 mL of Milli-Q water.

To obtain AuNR-MTX, 10 µL of a 100 mM solution of a previously reported MTX-containing Diels-Alder adduct in DMSO[48] were added to 10 mL of the previously prepared AuNRs and allowed to incubate while stirring for 2 h. The functionalized AuNRs-MTX were subsequently centrifuged twice at 13,000 × g for 15 min, resuspended, and stored at 4 °C prior to use. The supernatants were collected, and the presence of MTX containing adducts in the supernatant was quantified via UV–VIS using a standard calibration curve at 307 nm (Figure S1). The amount of adduct in the supernatants was subtracted from the initial amount to estimate the adduct concentration in the AuNR-MTX.

Characterization of the AuNRs and AuNR-MTX

AuNRs and AuNR-MTX were monitored via UV–Vis spectroscopy via a Lambda 25 spectrophotometer (Perkin Elmer, Waltham, MA, USA). The hydrodynamic diameter and Z potential were determined by a Zetasizer 3000 (Malvern Instruments, Malvern, UK) in a disposable DTS 1061 polycarbonate capillary cell DTS 1061, at 25 °C in triplicate in aqueous solution. The Smoluchowski approximation was used to measure the Z potential of the synthesized AuNPs. Transmission electron microscopy (TEM) images were acquired with a JEOL JEM-1010 microscope using Formvar carbon-coated copper microgrids; the size distribution was determined by measuring at least 50 particles.

Cell Culture

B16F10 cells were obtained from ATCC and cultured in RPMI culture medium containing 1% penicillin/streptomycin and 10% fetal bovine serum. MLG cells were cultured in DMEM containing 1% penicillin/streptomycin and 10% fetal bovine serum. The cultures were maintained under standard cell culture conditions at 37 °C and 5% CO_2. To obtain exosome-depleted FBS, commercial FBS was centrifuged at 100,000 × g for 8 h at 4 °C.

Preparation of EXOS and EXOS-AuNR-MTX

To obtain the HS-modified exosome-enriched fractions (EXOS), B16F10 cells were cultured in RPMI 1640 medium supplemented with 10% FBS until 40% confluence was reached. The medium was subsequently replaced with medium containing exosome-depleted FBS (10%) + DSPE-PEG-SH (1%). After 48 h, the medium was collected, and the exosomes were isolated via a sequential centrifugation protocol with some modifications.[37] Briefly, the medium was centrifuged to remove cell debris for 10 min at 300 × g and for 30 min at 2000 × g at 4 °C. The resulting supernatant was

filtered through a 0.22 μm pore filter and centrifuged at 100,000 × g for 2 h at 4 °C to isolate the EXOS. The protein amount in EXOs was quantified using a commercial micro-BCA kit following the manufacturer's recommendations. The particle amount was estimated by nanotracking analysis (NTA) in triplicate using a Nanosight® NS300 (Malvern, UK).

To obtain EXOS-AuNR-MTX, freshly prepared EXOS (100 μL, 1×10^{11} particles/mL) were incubated with 100 μL of a solution containing previously isolated AuNR-MTX (1×10^{12} particles/mL) with shaking at 4 °C for 24 h. Then, EXOS-AuNR-MTX were collected from the supernatant by centrifugation at 13,000 × g for 5 min. The final gold concentration in EXOS-AuNR-MTX was estimated by Graphite Furnace Atomic Absorption (GFAAS, ContrAA 800G-Analytic Jena, Germany) for in vivo studies.

EXOS and EXOS-AuNR-MTX were characterized by TEM using 1% uranyl acetate and 0.1% phosphotungstic acid. Briefly, a copper grid was deposited in a drop of the sample and allowed to interact for 2 min. Subsequently, the grid was washed with a drop of water for one min, stained with uranyl acetate or phosphotungstic acid for 30s, washed again and left to dry overnight. EXOS and EXOS-AuNR-MTX were also characterized by Cryo-TEM. EXOS and EXOS-AuNR-MTX were characterized by Western blotting in three independent experiments, to identify proteins commonly present in exosomes, such as Alix, TSG-101 and CD81.

Preparation of DiD- and DiR-labeled EXOS

For microscopy, EXOS and EXOS-AuNR-MTX were labeled with a DiD fluorescent probe. Alternatively, for in vivo biodistribution analysis, EXOS and EXOS-AuNR-MTX were labeled with DiR. Freshly isolated EXOs (100 μg of protein) were incubated at 4 °C for 30 min with 1 μL of a 1 μM solution of the fluorescent lipophilic tracers DiR or DiD. The labeled EXOS-DiR or EXOS-DiD exosomes were separated from the remaining lipophilic tracer using an Amicon filter and washed 2 times with PBS.

MTS Mitochondrial Activity Assays

To confirm the safety of the complete nanosystem in vitro, a cell viability experiment was performed. B16F10 cells (5×10^3 cells/well) were seeded in pretreated 96-well plates and allowed to attach for 24 h. Then, the medium was removed, and fresh medium containing EXOS-AuNR-MTX (1–10 μg protein) was added and cells were incubated for 24 h. Then, the medium was replaced with phenol red-free medium containing MTS/PMS (Promega), and the cells were incubated for 3 h. Subsequently, the absorbance of the culture medium at 490 nm was recorded using a microplate reader, and the cell viability was calculated compared with a control without treatment. Statistical analysis was performed with GraphPad Prism V9.3.1 and values averaged from n=4 experiments are presented with error bars representing the SEM. *Significant difference according to the Kruskal–Wallis test: **$p \leq 0.01$ compared with the medium control (Additional File 1).

Uptake Assessment by Fluorescence Microscopy

B16F10 or MLG cells (from ATCC), 5×10^3 cells/well, were seeded in 24-well, poly-L-lysine precoated glass-bottom culture dishes and allowed to attach for 24 h under standard culture conditions. The medium was then replaced with fresh medium containing the DiD-labeled treatments EXOS, EXOS-AuNR-MTX (5 μg of protein) and PBS (control) and incubated for 1, 3, 6 and 24 h. After treatment, the cells were washed with PBS, and fresh red phenol-free medium containing HOECHST and DiO (1 nM final concentration) was added for nuclear and membrane labeling, respectively. The cells were incubated for 30 min, washed 2 times with PBS, fixed in 4% PFA for 20 min and mounted on slides using Fluoromont montage solution for visualization. Fluorescence was detected using a BioTek Cytation 5 cell imaging multimode reader from Agilent (CA, USA). Hoechst in the cell nucleus was excited at 377 nm, and emission was recorded at 447 nm. The DiD from EXOS was excited at 628 nm, and the emission was recorded at 685 nm. Finally, DiO in the cell membranes was excited at 469 nm, and emission was recorded at 525 nm. Images were processed using BIOTEK software (CA, USA). The mean red fluorescence intensity was quantified and plotted ± SEM after treatment with EXOS or EXOS-AuNR-MTX in B16F10 and MLG cells, and significant differences were calculated using the Kruskal–Wallis test.

Animal Experiments

All mouse studies were performed in C57BL/6 mice following a bioethics protocol (22561-MED-UCH) approved by the Animal Ethics Committee (CICUA) of the Universidad de Chile. C57BL/6 mice were housed in polycarbonate cages in a temperature-controlled room at 20 °C under a 12-h light/dark cycle. Rat chow and filtered water were available *ad libitum*.

Metastasis Model and Biodistribution Analysis

Eight-week-old C57BL/6 mice were injected intravenously with 2×10^5 B16F10 cells (400 µL of saline solution or 0.9% NaCl). After 19 days, the mice were injected intravenously with 200 µL of the following treatments: PBS (control group), EXOS (50 µg protein, DiR-labeled), EXOS-AuNR-MTXs (50 µg protein, 1×10^{10} particles/mL AuNR, 0.9 ±0.18 µmol/mL MTX, DiR-labeled) or AuNR-MTX ($1x10^{10}$ particles/mL). After 24 h, the animals were anesthetized (2% isoflurane, via inhalation), shaved on the back and visualized in vivo using the In-Vivo FX PRO imaging system (Bruker, USA), as shown in the Additional File 1. The animals were then perfused with PBS, and the organs were visualized with an In-Vivo FX PRO (Bruker). The lungs were fixed with FEKETES fixing solution for 48 h at 4 °C, and black tissue was separated from normal lung tissue, lyophilized and weighed. The extent of metastasis was expressed as the percentage (%) of tumors/lung mass post-fixation (Additional File 1) as previously reported,[62] and significant differences in tumor percentage were estimated compared with that of PBS using the Kruskal–Wallis test. Organs were lyophilized and homogenized with a mortar, and the gold content was determined by Graphite Furnace Atomic Absorption Spectrometry (GFAAS, see conditions for detection in Table S1). Gold was quantified in the organs of the animals in all the experimental groups, but only in the AuNRs-MTX and EXOS-AuNR-MTX groups was the amount of gold quantified. The percentage of the injected dose per gram (%ID/g)[32] was calculated as follows:

$$\%\frac{\mathrm{ID}}{\mathrm{g}} = \frac{\text{total quantified gold (ng)}/\text{total gold in injected dose}}{\text{organ mass (g)}} \times 100$$

Statistical analysis for gold quantification was performed using GraphPad Prism V.9.3.1, and the Mann–Whitney test was used for multiple comparisons against the PBS control. In parallel, sections of the lung and liver were fixed in FEKETES, embedded in paraffin, and sectioned (5 µM) using a microtome for gold nucleation analysis and assessment of liver damage, respectively. These experiments were repeated four times (n=4 animals). To observe gold nucleation, a commercially available kit (Gold Enhancement™ Nanoprobes (NY, USA)) was used. At least five digital images were obtained per sample by light microscopy at 40–100× magnification with identical camera settings.

Results and Discussion

Characterization of AuNR-MTX and EXOS-AuNR-MTX

AuNR-MTX in each functionalization step as well as B16F10 EXOS and EXOS-AuNR-MTX-FAM were characterized using different techniques. Initially, the AuNRs-CTAB obtained were stabilized by the cationic surfactant CTAB, which is inherently toxic to cells. Therefore, the CTAB was then replaced by HS-PEG-COOH and HS-PEG-OMe on the surface before functionalization with the MTX-containing adduct. As shown in Figure 1 and Table 1, the freshly synthesized AuNRs-CTAB presented a characteristic plasmon peak at 799 nm, leading to a hypsochromic shift to 789 nm in the AuNRs and 786 nm in the AuNRs-MTX because of variations in the dielectric constant following surface functionalization.[63] The amount of MTX containing the adduct on the surface of the AuNRs-MTX was determined using a standard calibration curve, considering 49.800±10.000 molecules of adduct per AuNR (Figure S1). Additionally, the hydrodynamic diameter was determined to be 2 and 43 nm for the AuNRs-CTAB; 9 and 79 nm for the AuNRs; and 8 and 51 nm for the AuNR-MTX. An increase in diameter was observed after each step of functionalization (Figure 1, Table 1 and Figure S2), which is in agreement with previously reported studies, where the hydrodynamic diameter gradually increased following surface functionalization with PEG and small molecules.[23,29,34,35] Additionally, the Z potential was found to be +41 mV for the AuNRs-CTAB due to the presence of the cationic surfactant CTAB and $-12\ mV$ for the AuNRs and AuNR-MTX, following the displacement of the cationic CTAB by the negatively charged $PEG\text{-}COO^-$ and the neutral MTX-containing adduct in the functionalization steps (Figure 1, Table 1 and Figure S3).

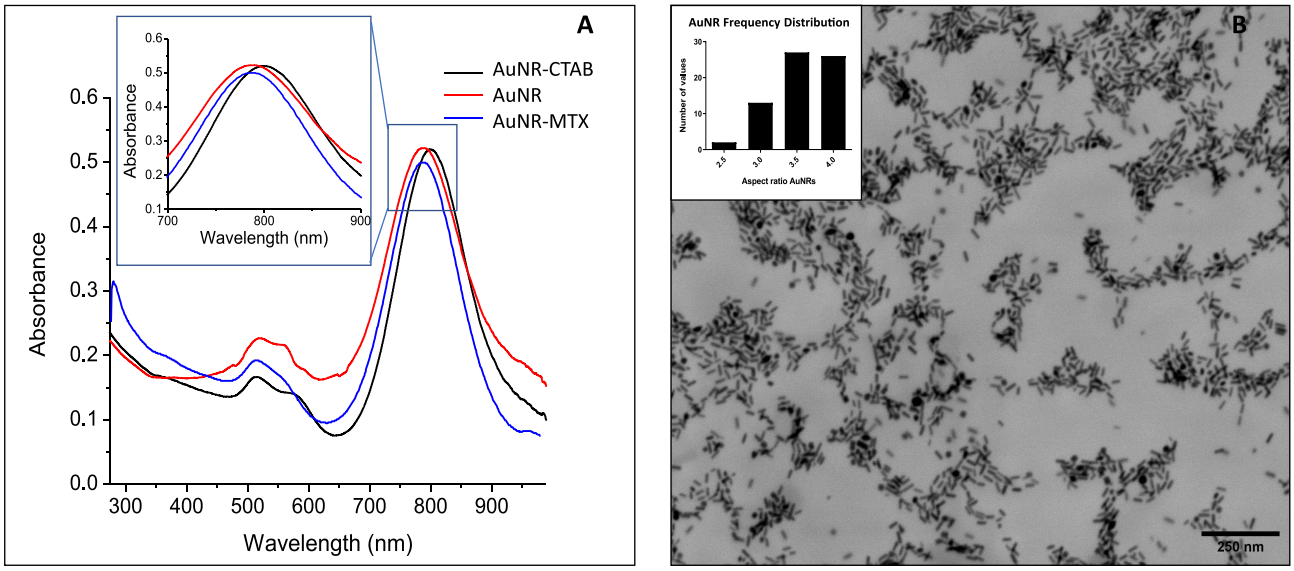

Figure 1 Characterization of the AuNRs-MTX following the functionalization steps: (**A**) UV–Vis-NIR spectrum showing plasmon displacement by functionalization; (**B**) TEM image of AuNRs with the size distribution inset.

These results are in agreement with previous studies, where the displacement of CTAB by PEG-COO^- on the surface resulted in negative zeta potential values.[23,29,34,35,64,65]

Fractions of enriched HS-modified vesicles (EXOS) were successfully obtained by ultracentrifugation. We confirmed the incorporation of thiol groups in the EXO-SH samples by comparing FT-IR spectra of control exosomes (without incubation with HS-DSPE-PEG) and EXOS samples (Figure S4). A peak in the 2300–2400 cm^{-1} range, corresponding to the thiol group, was found in the EXOS sample and this peak was absent in the spectrum of the control exosomes, which were not enriched with DSPE-PEG-SH. Additionally, the association between AuNR-MTX and EXOS at different EXOS:AuNR-MTX ratios was studied by NTA Analysis (Figure S5); notably, at a 1:1 ratio, the peak corresponding to the EXOS-AuNR-MTX complex is highly prevalent, indicating effective binding. However, at the 1:2 ratio, a smaller peak at 69 nm begins to emerge, and at the 1:5 ratio, this peak at 62 nm is most prevalent, suggesting the presence of excess, non-associated AuNR-MTX. These results indicate that higher AuNR-MTX concentrations beyond the 1:2 ratio increase dramatically the prevalence of non-bound nanoparticles. On the other hand, the results of TEM (Figure 2A) revealed circular or elliptical vesicles with diameters ranging from 80–150 nm. Additionally, Figures 2B and C show the presence of AuNR-MTX associated with EXOS in the EXOS-AuNR-MTX preparations. The appearance of EXOS and EXOS-AuNR-MTX was confirmed by Cryo TEM (Figure 2E and F). The mode of the diameter as determined by NTA

Table 1 Summary of the Physicochemical Characterization Results Showing That the Displacement of the Plasmon (λ_{max}) Increases with the Hydrodynamic Diameter, the Z Potential Varies as Functionalization Proceeds, and Finalizes Upon EXOS Functionalization with AuNR-MTX

	λ_{max} (nm)	Hydrodynamic Diameter (nm)		PDI	Z Potential (mV)
AuNR-CTAB	799	2±0.1	43±0.9	0.5	41±3
AuNR	789	9±2.6	79±3.0	0.5	−12±3
AuNR-MTX	786	8±1.2	51±2.5	0.6	−12±4
EXOS	-	-	258±27	0.4	−10±1
EXOS-AuNR-MTX	786	-	396±30	0.3	−14±2

https://doi.org/10.2147/IJN.S513628

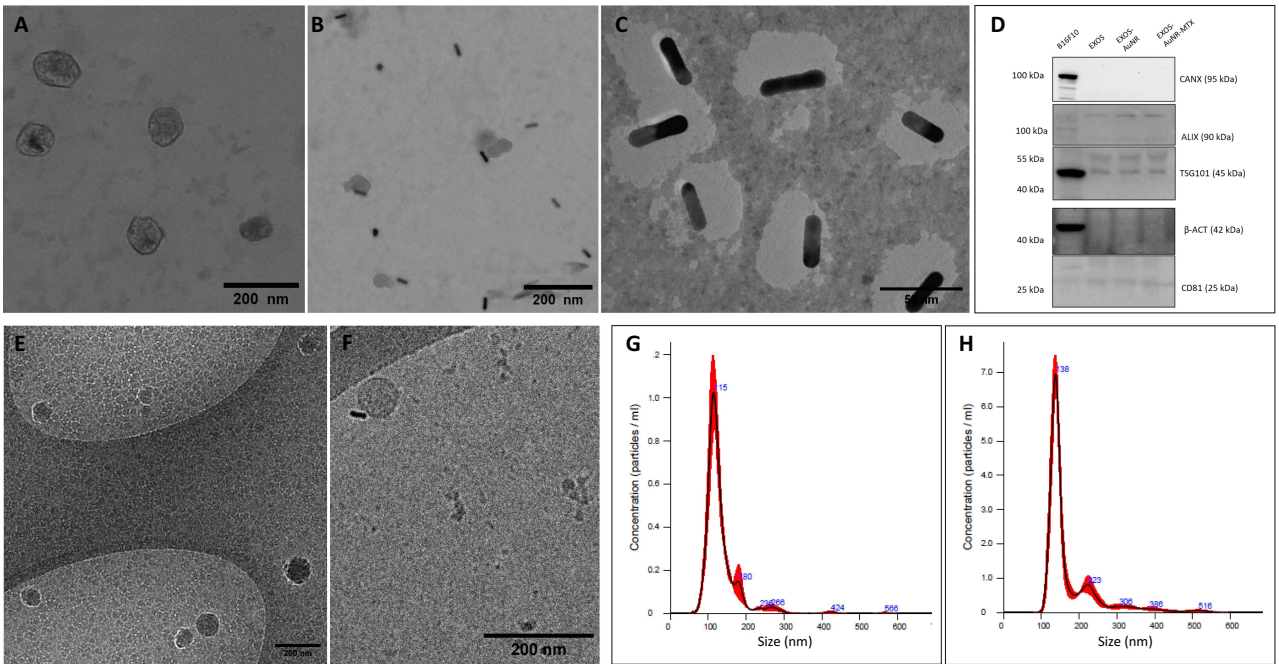

Figure 2 Representative TEM images of glutaraldehyde-fixed EXOS (**A**) and EXOS-AuNR-MTX (**B**) samples stained with 0.1% phosphotungstic acid. TEM image of nonfixed EXOS-AuNR-MTX stained with 1% uranyl acetate (**C**). In A-B, the dark circles (positive staining) represent the EXOS; in C, the light circular areas (negative staining) represent EXOS. Western blot showing the absence of CANX (ER marker) and the presence of markers Alix, TSG-101 and CD81 in the EXOS, EXOS-AuNR, EXOS-AuNR -MTX and cell lysates (**D**). Cryo TEM images of EXOS (**E**) and EXOS-AuNR-MTX (**F**). NTA showing the mode of size: 114.4±2.7 nm for EXOS (**G**) and 137.4±1.0 nm for EXOS-AuNR-MTX (**H**). Scale bars: (**A, B, E** and **F**) 200 nm; (**C**) 500 nm.

was found to be 114 nm for EXOS and 138 nm for EXOS-AuNR-MTX (Figure 2G and H), which agrees with the expected increase in diameter following the association between AuNR-MTX and EXOS. We then detected the proteins commonly present in the exosomes by Western blotting. The exosome markers Alix, TSG-101 and CD81 were observed in lysates of EXOS, EXOS-AuNR and EXOS-AuNR-MTX. Alternatively, calnexin, (CANX), an endoplasmic reticulum marker, was not detected in the isolated EXOS with or without the inclusion of AuNRs, indicating that the exosome preparations were not contaminated by components of the endoplasmic reticulum.

The stability of the nanoconjugate EXOS-AuNR-MTX was evaluated under different storage conditions (4°C, −20°C, −80°C, and −80°C with 5% DMSO as a cryopreservant), and the results have been included in Figure S6. One month after the synthesis of the nanosystem, the size distribution remained similar, and no detectable peak corresponding to free AuNRs was observed, suggesting that the conjugates remained stable over time. Additionally, we demonstrated the safety of the complete EXOS-AuNR-MTX nanosystem in B16F10 cells after 24 h of treatment using a cell viability assay (Figure S7). No significant effects on B16F10 cell viability were detected under the conditions evaluated (1–10 µg of protein). These results suggest that we were able to generate EXOS from B16F10 cells loaded with AuNR-MTX for potential bioapplications.

Cellular Uptake of B16F10 EXOS in vitro

In order to determine whether the uptake of B16F10 EXOS and EXOS-AuNR-MTX is cell-type specific, we compared the uptake by B16F10 cells with that observed for MLG cells (normal mouse lung cells) under similar culture conditions, as shown in Figure 3 (40X objective) and Figure S8 (20X objective). The EXOS and EXOS-AuNR-MTX were labeled with the lipophilic tracer DiD (red channel), and the membrane was labeled with the lipophilic tracer DiO (green channel), in order to identify the cell membrane and to determine whether the localization of the EXOS was intracellular following uptake. As shown in Figures 3 and S8, similar patterns of accumulation for EXOS and EXOS-AuNR were observed over time, suggesting that the incorporation of AuNR-MTX did not affect the uptake in the cell lines. EXOS and EXOS-AuNR-MTX were observed to be bound and internalized into the cytoplasm of B16F10 cells in a time-

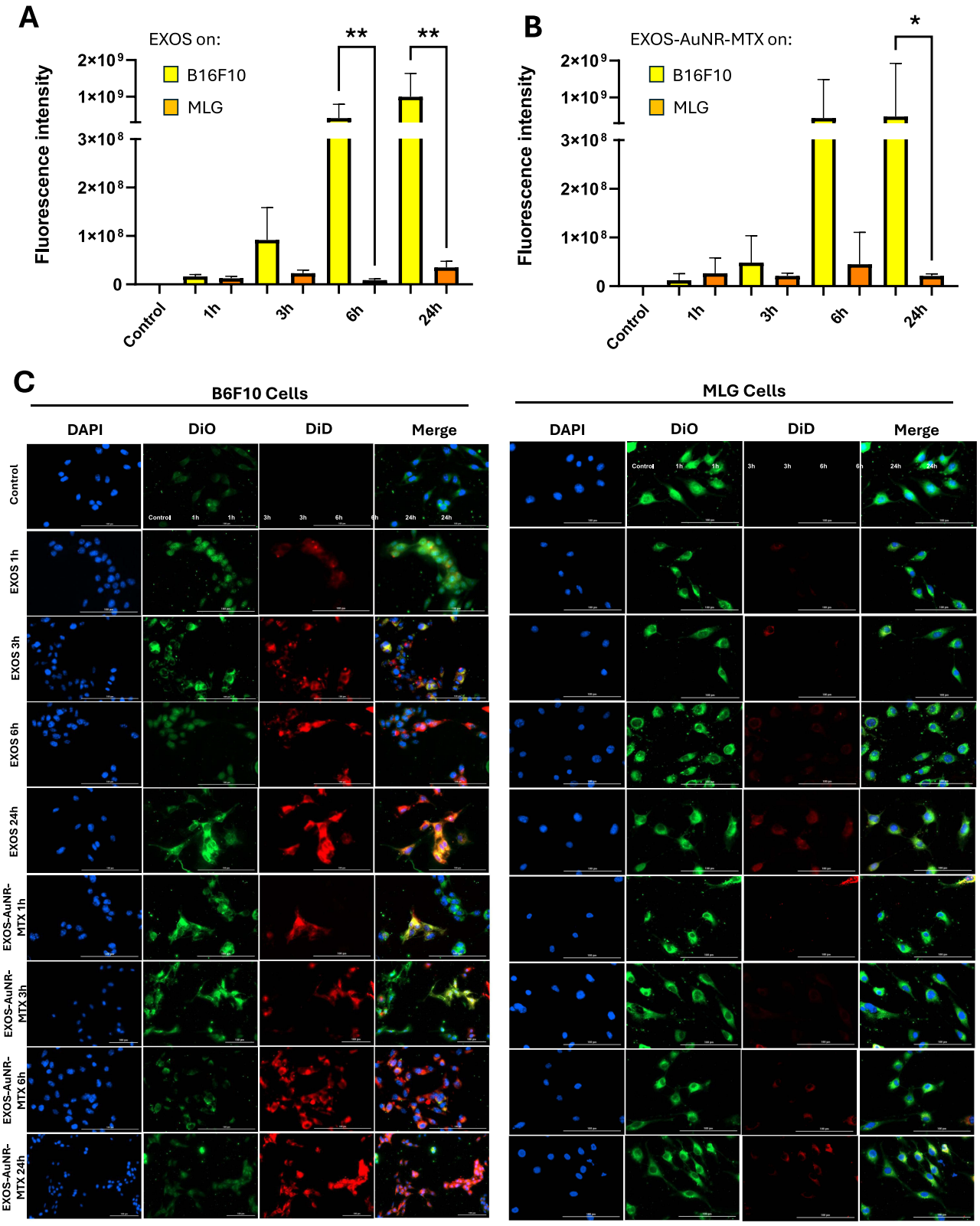

Figure 3 Uptake by cells of EXOS and EXOS-AuNR-MTX. Uptake by B16F10 cells was elevated compared to MLG cells. Cells were incubated with DiD-labeled EXOS and EXOS-AuNR-MTX (5 μg of protein) for 1, 3, 6 or 24 h and analyzed by fluorescence microscopy. Mean red-fluorescence intensity quantification ± SEM after treatment with EXOS (**A**) and EXOS-AuNR-MTX (**B**) for B16F10 cells (yellow) and MLG cells (Orange). Significant differences according to the Kruskal–Wallis test are indicated: *p≤0.05, **p ≤ 0.01. (**C**) Microscopy images of cell internalization acquired at 40X. The DiD-labeled samples are shown in red; the membranes were stained with DiO in green, and the nuclei are shown in blue following Hoechst staining.

https://doi.org/10.2147/IJN.S513628

dependent manner. The uptake increased from 1 to 6 h but did not increase further after 24 h. Interestingly, at earlier time points (1 h and 3 h), the EXOS and EXOS-AuNR-MTX accumulation in B16F10 cells and MLG cells did not show substantial differences. However, after 6 and 24 h, the fluorescence intensity was notably higher for B16F10 than MLG cells. These findings suggest that exosome uptake by B16F10 cells increases over time, whereas this is not the case for MLG cells, indicating a preference for the uptake of exosomes by their cells of origin after extended incubation periods (6 and 24 h). In previous studies, the specificity and time-dependent uptake of B16F10 exosomes by cells were reported.[62,66–68] Additionally, the cell-specific uptake of exosomes by other cell lines has been described,[69–73] in agreement with our results.

Lung Metastasis Model

A lung melanoma metastasis model was established by intravenous injection of B16F10 cells into recipient syngeneic C57BL/6 mice (Figure S9) as reported previously.[62,74] The animal survival rate was 100% in all the experiments, and the body weight was not significantly altered by any of the treatments (Figure S10). The fact that no changes in body weight were observed throughout the study suggests that the nanoformulations do not induce acute toxicity. This observation is consistent with previous studies, in which the potential toxicity of exosome administration was assessed by monitoring body weight before and after treatment. No significant variations were reported, further supporting the safety of exosome-based therapies.[75–78] In addition, the percentage of tumors in the mouse lungs was approximately 20% in all the conditions evaluated (Figure S11), as previously reported for this metastasis model.[62,74]

Representative lung sections obtained from the lungs of C57BL/6 mice inoculated with PBS, EXOS, AuNR-MTX or EXOS-AuNR-MTX are shown (Figure 4A–D). For all the animals, metastatic nodules were found in the lungs and parenchyma (Figure 4 and Additional File 1). In these tumors, the melanoma cells were characterized by the expression of melanin and their typical cell morphology (blue arrows). No notable differences were observed following the different treatments.

Additionally, we assessed liver cytotoxicity following the different treatments, given that nanoparticles generally accumulate to a considerable extent in the liver. The results revealed no histopathological abnormalities, such as inflammation, necrosis, or cell damage, indicating that EXOS-AuNR-MTX do not induce liver toxicity under the experimental conditions used (Figure 4E–H).

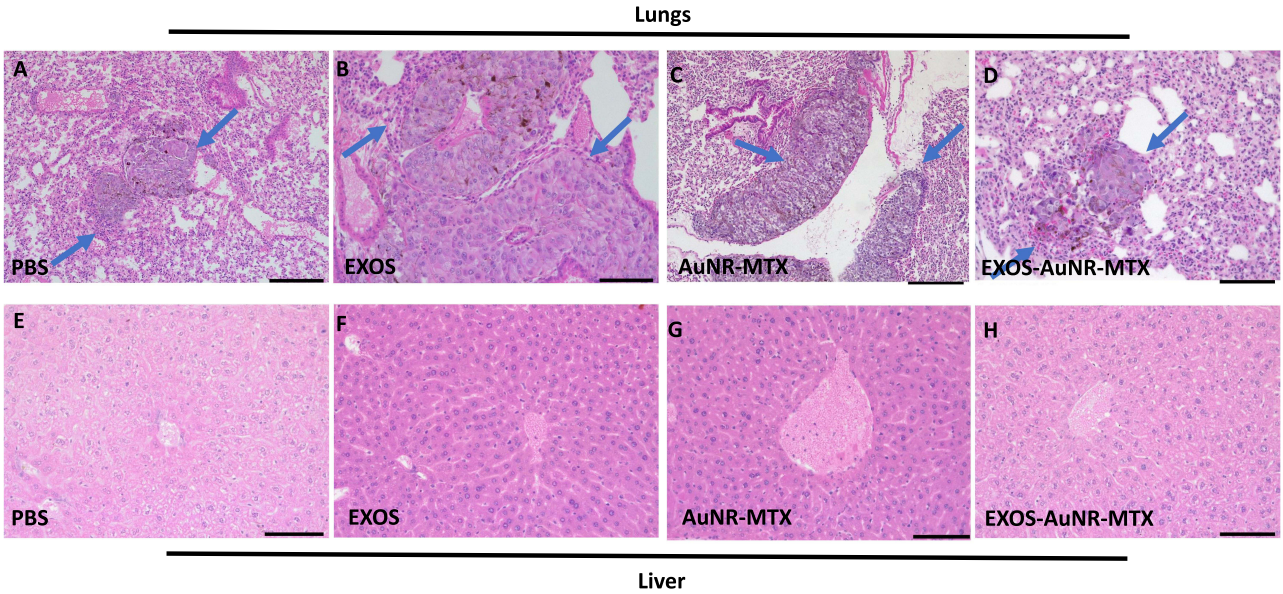

Figure 4 Histological analysis of tumor growth and metastasis of B16F10 cells in the lungs (**A–D**) of C57BL/6 mice: B16F10 metastatic nodules showing melanin expression and melanoma cell morphology (blue arrows). Histological sections of liver (**E–H**) showing no hepatic cell abnormalities after 24 h of treatment. Mice (n=4) were treated with PBS (A, E), EXOS (B, F), AuNR-MTX (**C** and **G**), or EXOS-AuNR-MTX (**D** and **H**) (50 μg protein EXOS, 1×10^{10} particles/mL AuNR, 0.9±0.18 μmol/mL MTX). Hematoxylin and eosin staining; magnification bar: 100 μm.

Biodistribution of EXOS and EXOS-AuNR-MTX in the Lung Metastasis Model in vivo

The treatments PBS, EXOS, AuNR-MTX and EXOS-AuNR-MTX were administered and the biodistribution was studied 24 h after intravenous injection into the mice. For visualization in vivo, the backs of the animals were shaved to confirm the delivery of the DiR-labeled EXOS and EXOS-AuNR-MTX to the lungs, at λ_{exc}=720 nm and λ_{em}=790 nm, respectively (Figure S12). The presence of the EXOS in the lungs following the treatments was detected in vivo (Figure S12) and confirmed ex vivo (Figure S13). Fluorescence in the lungs ex vivo due to the presence of EXOS or EXOS-AuNR-MTX was significantly higher than for lungs from PBS and AuNR-MTX control animals.

Once we confirmed the presence of the EXOS in the lungs of the animals by fluorescence, the total content of gold was determined by GFAAS (Figure S14) in the animals treated with AuNR-MTX or EXOS-AuNR-MTX. Values shown were calculated as the percentage (%) of the injected dose per gram of the respective tissues %ID/g, Figure 5 (materials and methods 3.1). Similar patterns of biodistribution of AuNRs-MTX and EXOS-AuNR-MTX were found in heart, kidney, liver, and spleen. In contrast, significantly higher amounts of gold were found in the tumors following the EXOS-AuNR-MTX treatment, which can be attributed to the targeting effect of the exosomes. As expected, and previously reported, liver and spleen retain most of the administered nanomaterials, decreasing the delivery to the tumors.[29,62,79–81] In the liver, Kupffer cells, hepatic B cells and liver sinusoidal endothelial cells are the main cells responsible of retention of nanoparticles, whereas macrophages are responsible for most of the retention observed in the spleen.[82]

Interestingly, the exosomes combined with AuNR-MTX in EXOS-AuNR-MTX accumulated to a greater extent in the tumors, compared to AuNR-MTX alone. Specifically, the %ID/g of tissue increased 11 times for EXOS-AuNR-MTX (5.5% average) compared to nanoparticles AuNR-MTX alone (0.5% average). This represents an important finding, given that the accumulation of AuNRs alone in tumor tissues is estimated to be less than 1% of the administered dose.[32,33] It is also interesting to note that although there appears to be an increase in gold accumulation in non-target cells in the lungs, this may in fact be due to the presence of tumors smaller than 1 mm in size (see histological images in

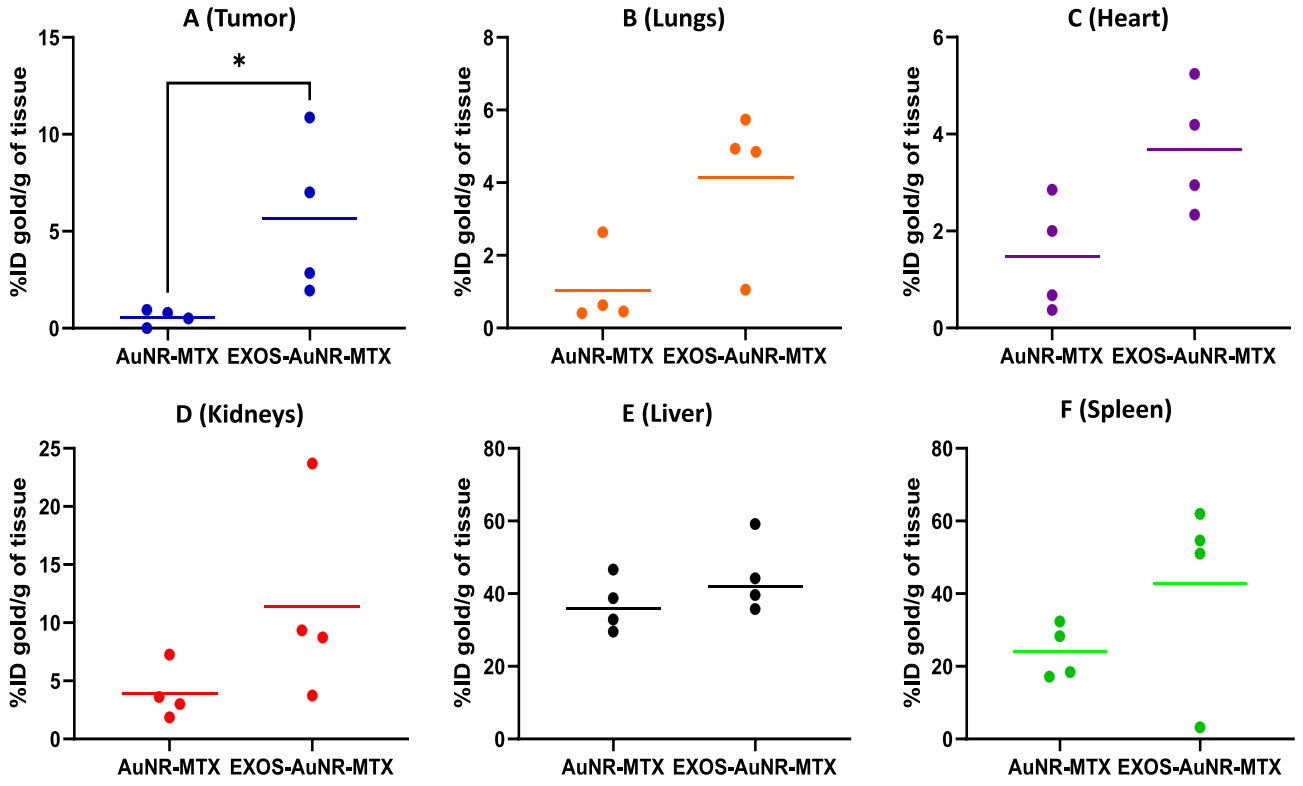

Figure 5 Accumulation of gold particles (percentage of injected gold per gram of tissue %ID/g) in the tumors (**A**) and different organs (**B**-**F**) ex vivo in the mice after 24 h treatment with AuNR-MTX or EXOS-AuNR-MTX (50 μg protein, 1×1010 particles/mL AuNR, 0.9±0.18 μmol/mL MTX). Remarkably, significant differences in the gold concentration were found only in the tumors (**A**), whereby higher gold concentrations were observed following the treatment with EXOS-AuNR-MTX. Significant differences according to t-test are indicated: *p≤0.05.

https://doi.org/10.2147/IJN.S513628

Figures 4 and S15–S18), which are difficult to separate completely from the rest of the lung tissue. Therefore, since increased levels were found in the lung, a histological study was performed in order to confirm the selective accumulation of the gold in tumor rather than healthy lung tissue sites.

Selective Accumulation of the EXOS-AuNR-MTX in Metastatic Lung Nodules

To verify the accumulation of AuNRs in the lungs of the animals, histological sections were prepared to evaluate the distribution of the gold in the lung tissue using the gold enhancement commercial kit. The procedure enriches the gold nucleation in the zones where gold accumulation exists, making the AuNRs accumulation visible as blue stains. As shown in Figures 6A,B and S15–S17, no accumulation of gold was observed for the controls PBS or EXOS. Interestingly, the accumulation of the AuNR-MTX in lungs was not high enough to be detected by this technique. Remarkably, the accumulation of gold in the lungs of the animals treated with EXOS-AuNR-MTX was clearly detected as blue staining (Figure 6C–F and Figure S18). Also, the accumulation of the gold was found to be selective and enhanced in metastatic tumor sites (colocalization with brownish melanin spots and disorganized cell structure). Meanwhile, no accumulation was detected in the healthy tissues (pink color with eosin staining, organized cell structure). The increased accumulation of the EXOS-AuNR-MTX is likely attributable to higher retention and residence in the tumors, due to the homing properties of the exosomes and the vascularization of the tumors.[60,62,83,84] Therefore, the presence of the EXOS in EXOS-AuNR-MTX increased the specific accumulation of the nanosystem in the metastatic melanoma tumors present in the lungs.

The efficient accumulation of EXOS-AuNR-MTX in tumor tissues can be attributed to a combination of biological and physicochemical factors that enhance selective targeting and retention within the tumor microenvironment. First, the enhanced permeability and retention (EPR) effect contributes to the passive accumulation of the nanoconjugates in tumor tissues. The irregular vasculature of solid tumors, characterized by leaky blood vessels and impaired lymphatic drainage, allows nanoparticles to extravasate and accumulate at the tumor site.[60,62] Given the nanoscale dimensions of EXOS-AuNR-MTX, they can efficiently exploit the EPR effect, particularly in pulmonary metastatic lesions, where tumor-

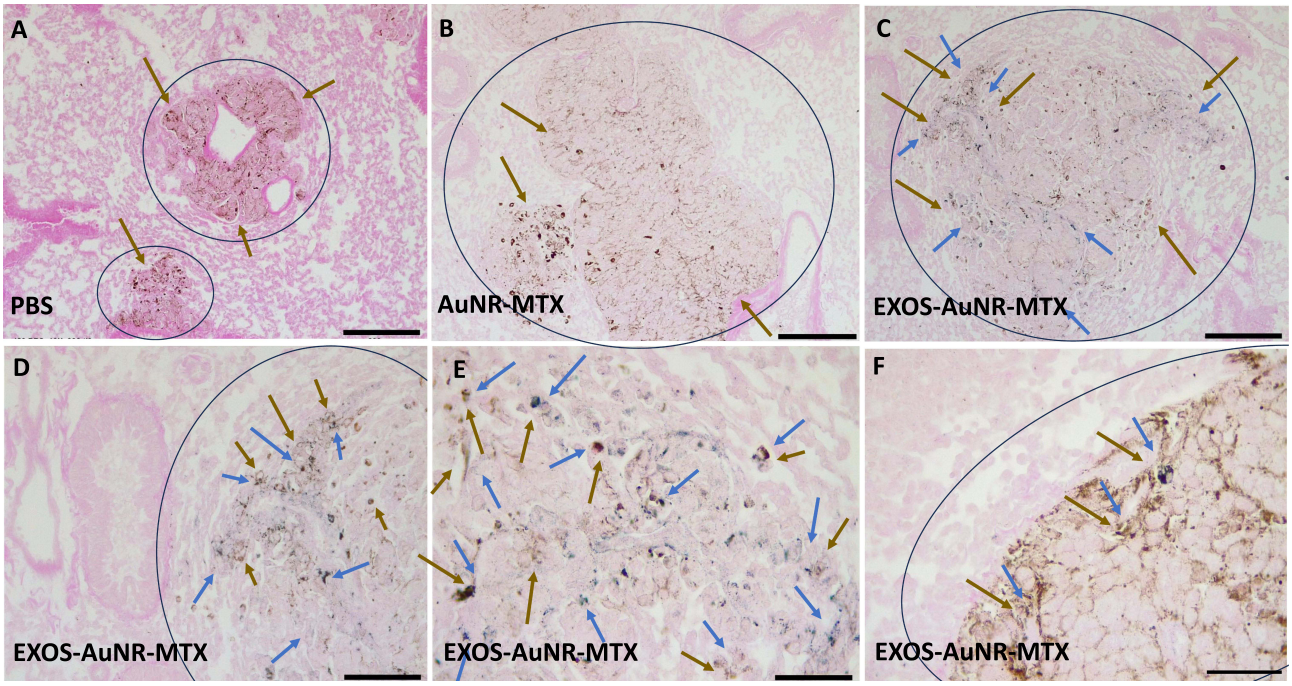

Figure 6 Histological detection of AuNR loaded exosomes in small metastatic nodules (blue circles) by gold enhancement in the lungs of mice treated 24 h with PBS control (**A**), AuNR-MTX (**B**), EXOS-AuNR-MTX (**C**–**F**), (50 μg protein, 1×10^{10} particles/mL AuNR, 0.9±0.18 μmol/mL MTX). Eosin (Pink), gold enhancement (blue), melanin (brown). Images show the colocalization of the AuNRs (blue arrows) and melanin-containing metastatic nodules (brown arrows) exclusively following the treatment with EXOS-AuNR-MTX (blue arrows). Magnification bar: (**A**–**C**) 200μm 10X, (**D**) 100 μm 20X, (**E** and **F**) 50 μm 40X.

associated vascular abnormalities are pronounced.[83,84] Second, the homing selectivity of exosomes plays a critical role in directing the nanosystem to the tumor site. The exosomes utilized in this study are derived from B16F10 melanoma cells, the same cell line used to generate tumors in the animal model. Since exosomes retain molecular markers and membrane components from their parental cells, they exhibit an affinity for recipient cells of the same cell line. This recognition pattern facilitates the preferential accumulation of EXOS-AuNR-MTX in B16F10-derived tumors. Third, the folate receptor (FR)-mediated endocytosis further enhances cellular internalization of the nanosystem. Methotrexate (MTX), a folic acid analog, is conjugated to the surface of AuNRs, enabling interaction with folate receptors, which are overexpressed in cancer cells. This ligand-receptor interaction promotes active targeting and receptor-mediated uptake, thereby increasing intracellular delivery of the nanoconjugates.

Additionally, the intercellular communication function of exosomes may also play a role in the enhanced tumor targeting of EXOS-AuNR-MTX, since exosomes naturally mediate the transfer of biomolecules between cells, a process that is particularly active within the tumor microenvironment.[84] The interaction between tumor-derived exosomes and recipient cancer cells may facilitate increased uptake through membrane fusion or receptor-mediated endocytosis,[83] further promoting the intracellular accumulation of EXOS-AuNR-MTX. These mechanisms, synergistically enhance the selective accumulation of EXOS-AuNR-MTX in tumor, underscoring their potential as an efficient nanoplatform for targeted cancer therapy.

Conclusion

In this study, we successfully developed and fully characterized EXOS-AuNR-MTX, demonstrating their safety and preferential accumulation in B16F10 melanoma cells compared to other cell lines in vitro. In an in vivo metastatic melanoma lung model, the nanosystem exhibited a favorable biodistribution profile, with 5.5% of the injected AuNR dose accumulating in tumor tissues, a significant increase compared to the 1% typically reported for AuNRs. Notably, histological analysis confirmed that AuNRs selectively accumulated in tumor vessels and nodules rather than healthy tissues, highlighting the tumor-targeting efficiency of this approach.

The efficient accumulation of EXOS-AuNR-MTX in tumors can be attributed to the synergistic effects of exosomal homing selectivity, the enhanced permeability and retention (EPR) effect, folate receptor-mediated endocytosis, and exosome-mediated intercellular communication, collectively enhancing tumor targeting and intracellular uptake. These findings provide valuable insights to the design of nanoplatforms that exploit the natural properties of exosomes for targeted drug delivery. The scientific significance of this study resides in showing that tumor-derived exosomes can be exploited to improve the biodistribution and tumor accumulation of gold nanorods, offering a promising strategy for metastatic melanoma treatment. This innovative approach enhances the selective delivery of cytotoxic agents, such as MTX, potentially reducing off-target effects and improving therapeutic efficacy.

However, certain limitations should be addressed in the future. While the study provides strong evidence for tumor accumulation and selectivity, additional research is needed to evaluate long-term biodistribution and the therapeutic efficacy of the nanosystem in extended preclinical models. Future studies should also assess their potential clinical translation in other cancer models.

Overall, this study presents a novel exosome-based strategy to improve the accumulation of gold nanoparticles in metastatic melanoma lung tumors, as a strategy to facilitate future advances in targeted nanomedicine.

Acknowledgments

This research was funded by grants FONDECYT Postdoc 3220587 (KB), FONDECYT 1230303 (EA), FONDAP 15130011, FONDAP Continuación 1523A0008 (AFGQ, MK), Fondecyt 1211482 (MK) Fondecyt 1251140 (MK), and 1210644 (AFGQ).

Disclosure

The author(s) report no conflicts of interest in this work. This manuscript was made available online ahead of publication at: https://www.researchsquare.com/article/rs-5399241/v1

References

1. Hanahan D, Weinberg RA. Hallmarks of cancer: the next generation. *Cell*. 2011;144:646–674. doi:10.1016/j.cell.2011.02.013
2. Sharma P, Diergaarde B, Ferrone S, Kirkwood JM, Whiteside TL. Melanoma cell-derived exosomes in plasma of melanoma patients suppress functions of immune effector cells. *Sci Rep*. 2020;10:1–11. doi:10.1038/s41598-019-56847-4
3. Sato K, Nagaya T, Nakamura Y, et al. Near infrared photoimmunotherapy prevents lung cancer metastases in a murine model. *Oncotarget*. 2015;6:19747–19758. doi:10.18632/oncotarget.3850
4. Guerrero S, Inostroza-Riquelme M, Contreras-Orellana P, et al. Curcumin-loaded nanoemulsion: a new safe and effective formulation to prevent tumor reincidence and metastasis. *Nanoscale*. 2018;10:22612–22622. doi:10.1039/C8NR06173D
5. Zhao Y, Park S-Y, Nishio T, et al. Targeted delivery of doxorubicin by nano-loaded mesenchymal stem cells for lung melanoma metastases therapy. *Sci Rep*. 2017;7:1–12. doi:10.1038/s41598-016-0028-x
6. Huang CY, Ju DT, Chang CF, Muralidhar Reddy P, Velmurugan BK. A review on the effects of current chemotherapy drugs and natural agents in treating non-small cell lung cancer. *Biomed*. 2017;7:12–23.
7. Durosini I, Janssens R, Arnou R, et al. Patient preferences for lung cancer treatment: a qualitative study protocol among advanced lung cancer patients. *Front Public Health*. 2021;9:1–10.
8. Lee YT, Tan YJ, Oon CE. Molecular targeted therapy: treating cancer with specificity. *Eur J Pharmacol*. 2018;834:188–196. doi:10.1016/j.ejphar.2018.07.034
9. Jain S, Hirst DG, O'Sullivan JM. Gold nanoparticles as novel agents for cancer therapy. *Br J Radiol*. 2012;85:101–113. doi:10.1259/bjr/59448833
10. Yhee JY, Son S, Son S, Joo MK, Kwon IC. The EPR Effect in Cancer Therapy. In: *Cancer Targeted Drug Delivery: An Elusive Dream*. 2013:621–632. doi:10.1007/978-1-4614-7876-8
11. Wicki A, Witzigmann D, Balasubramanian V, Huwyler J. Nanomedicine in cancer therapy: challenges, opportunities, and clinical applications. *J Control Release*. 2015;200:138–157. doi:10.1016/j.jconrel.2014.12.030
12. Xie X, Shao X, Ma W, et al. Overcoming drug-resistant lung cancer by paclitaxel loaded tetrahedral DNA nanostructures. *Nanoscale*. 2018;10:5457–5465. doi:10.1039/C7NR09692E
13. Almada M, Leal-Martínez BH, Hassan N, et al. Photothermal conversion ef fi ciency and cytotoxic effect of gold nanorods stabilized with chitosan, alginate and poly (vinyl alcohol). *Mater Sci Eng C*. 2017;77:583–593. doi:10.1016/j.msec.2017.03.218
14. Bolaños K, Celis F, Garrido C, et al. Adsorption of bovine serum albumin on gold nanoprisms: interaction and effect of NIR irradiation on protein Corona. *J Mater Chem B*. 2020;8:8644–8657. doi:10.1039/D0TB01246G
15. Sánchez C, Serrano JJ, Mina A, Ramírez N, Del Pozo F. A method to obtain the thermal parameters and the photothermal transduction efficiency in an optical hyperthermia device based on laser irradiation of gold nanoparticles. *Nanoscale Res Lett*. 2014;9:441. doi:10.1186/1556-276X-9-441
16. Chen H, Shao L, Ming T, et al. Understanding the photothermal conversion efficiency of gold nanocrystals. *Small*. 2010;6:2272–2280. doi:10.1002/smll.201001109
17. Guo A, Fu Y, Wang G, Wang X. RSC advances diameter effect of gold nanoparticles on photothermal conversion for solar steam generation. *RSC Adv*. 2017;7:4815–4824. doi:10.1039/C6RA26979F
18. Chiu HT, Chen C-H, Li M-L, et al. Bioprosthesis of core-shell gold nanorod/serum albumin nanoimitation: a half-native and half-artificial nanohybrid for cancer theranostics. *Chem Mater*. 2018;30:729–747. doi:10.1021/acs.chemmater.7b04127
19. Chen H, Shao L, Li Q, Wang J. Gold nanorods and their plasmonic properties. *Chem Soc Rev*. 2013;42:2679–2724. doi:10.1039/C2CS35367A
20. Zhang Z, Wang J, Nie X, et al. Near infrared laser-induced targeted cancer therapy using thermoresponsive polymer encapsulated gold nanorods. *J Am Chem Soc*. 2014;136:7317–7326. doi:10.1021/ja412735p
21. Huang H, Lovell JF. Advanced functional nanomaterials for theranostics. *Adv Funct Mater Theranostics*. 2017;27:1603524. doi:10.1002/adfm.201603524
22. Weissleder R. News and views: a clearer vision for in vivo imaging. *Nat Biotechnol*. 2001;19:316–317. doi:10.1038/86684
23. Vetterlein C, Vásquez R, Bolaños K, et al. Exploring the influence of Diels–Alder linker length on photothermal molecule release from gold nanorods. *Colloids Surf B Biointerfaces*. 2018;166:323–329. doi:10.1016/j.colsurfb.2018.03.021
24. Mooney R, Schena E, Zhumkhawala A, Aboody KS, Berlin JM. Internal temperature increase during photothermal tumour ablation in mice using gold nanorods. Proceedings Annual International Conference of IEEE Engineering in Medicine and Biology Society. EMBS. 2015 November; 2015: 2563–2566.
25. Callaghan C, Peralta D, Liu J, et al. Combined treatment of tyrosine kinase inhibitor-labeled gold nanorod encapsulated albumin with laser thermal ablation in a renal cell carcinoma model. *J Pharm Sci*. 2016;105:284–292. doi:10.1016/j.xphs.2015.11.017
26. Peralta DV, Heidari Z, Dash S, Tarr MA. Hybrid paclitaxel and gold nanorod-loaded human serum albumin nanoparticles for simultaneous chemotherapeutic and photothermal therapy on 4T1 breast cancer cells. *ACS Appl Mater Interfaces*. 2015;7:7101–7111. doi:10.1021/acsami.5b00858
27. Wang X, Li J, Kawazoe N, Chen G. Photothermal ablation of cancer cells by albumin-modified gold nanorods and activation of dendritic cells. *Materials*. 2018;12:31. doi:10.3390/ma12010031
28. Vines JB, Yoon JH, Ryu NE, Lim DJ, Park H. Gold nanoparticles for photothermal cancer therapy. *Front Chem*. 2019;7:1–16. doi:10.3389/fchem.2019.00167
29. Jara-Guajardo P, Morales-Zavala F, Bolaños K, et al. Differential detection of amyloid aggregates in old animals using gold nanorods by computerized tomography: a pharmacokinetic and bioaccumulation study. *Int J Nanomed*. 2023;18:8169–8185. doi:10.2147/IJN.S435472
30. Jokerst JV, Cole AJ, Van de Sompel D, Gambhir SS. Gold nanorods for ovarian cancer detection with photoacoustic imaging and resection guidance via Raman imaging in living mice. *ACS Nano*. 2012;6:10366–10377. doi:10.1021/nn304347g
31. Deinavizadeh M, Kiasat AR, Shafiei M, et al. Synergistic chemo-photothermal therapy using gold nanorods supported on thiol-functionalized mesoporous silica for lung cancer treatment. *Sci Rep*. 2024;14:1–12. doi:10.1038/s41598-024-54778-3
32. Price LSL, Stern ST, Deal AM, Kabanov AV, Zamboni WC. A reanalysis of nanoparticle tumor delivery using classical pharmacokinetic metrics. *Sci Adv*. 2020;6:1–9. doi:10.1126/sciadv.aay9249
33. Wilhelm S, Tavares AJ, Dai Q, et al. Analysis of nanoparticle delivery to tumours. *Nat Rev Mater*. 2016;1:13–17. doi:10.1038/natrevmats.2016.14

34. Riveros AL, Eggeling C, Riquelme S, et al. Improving cell penetration of gold nanorods by using an amphipathic arginine rich peptide. *Int J Nanomed*. 2020;15:1837–1851. doi:10.2147/IJN.S237820
35. Bolaños K, Sánchez-Navarro M, Tapia-Arellano A, et al. Oligoarginine peptide conjugated to BSA improves cell penetration of gold nanorods and nanoprisms for biomedical applications. *Int J Nanomed*. 2021;13:1204.
36. Encinas-Basurto D, Ibarra J, Juarez J, et al. Hybrid folic acid-conjugated gold nanorods-loaded human serum albumin nanoparticles for simultaneous photothermal and chemotherapeutic therapy. *Mater Sci Eng C*. 2018;91:669–678. doi:10.1016/j.msec.2018.06.002
37. Wang J, Dong Y, Li Y, et al. Designer exosomes for active targeted chemo-photothermal synergistic tumor therapy. *Adv Funct Mater*. 2018;28:1–14.
38. Lodhi MS, Khalid F, Khan MT, et al. A novel method of magnetic nanoparticles functionalized with anti-folate receptor antibody and methotrexate for antibody mediated targeted drug delivery. *Molecules*. 2022;27:261. doi:10.3390/molecules27010261
39. Yücel O, Şengelen A, Emik S, et al. Folic acid-modified methotrexate-conjugated gold nanoparticles as nano-sized trojans for drug delivery to folate receptor-positive cancer cells. *Nanotechnology*. 2020 28;31(35):355–101. doi:10.1088/1361-6528/ab9395):355101
40. Al-Nemrawi N, Altawabeyeh R, Darweesh RS, Alnabulsi S. Coating methotrexate-PLGA nanoparticles with folic acid-chitosan conjugate for cancer targeting. *Pharmacia*. 2024;71:1–9. doi:10.3897/pharmacia.71.e120072
41. Du Z, Sun J, Bader CA, et al. Synthesis, photophysical and cellular characterisation of folate and methotrexate labelled luminescent lanthanide complexes. *J Inorg Biochem*. 2018;178:32–42. doi:10.1016/j.jinorgbio.2017.10.003
42. Li D, Zhang M, Xu F, et al. Biomimetic albumin-modified gold nanorods for photothermo-chemotherapy and macrophage polarization modulation. *Acta Pharm Sin B*. 2018;8:74–84. doi:10.1016/j.apsb.2017.09.005
43. Liu J, Abshire C, Carry C, et al. Nanotechnology combined therapy: tyrosine kinase-bound gold nanorod and laser thermal ablation produce a synergistic higher treatment response of renal cell carcinoma in a murine model. *BJU Int*. 2017;119:342–348. doi:10.1111/bju.13590
44. Yeo ELL, Cheah JU-J, Neo DJH, et al. Exploiting the protein Corona around gold nanorods for low-dose combined photothermal and photodynamic therapy. *J Mater Chem B*. 2017;5:254–268. doi:10.1039/C6TB02743A
45. Deng Y, Wang Y, Cherian C, et al. Synthesis and discovery of high affinity folate receptor-specific glycinamide ribonucleotide formyltransferase inhibitors with antitumor activity. *J Med Chem*. 2008;51:5052–5063. doi:10.1021/jm8003366
46. Spinella MJ, Brigle KE, Sierra EE, Goldman ID. Distinguishing between folate receptor-α-mediated transport and reduced folate carrier-mediated transport in L1210 leukemia cells. *J Biol Chem*. 1995;270:7842–7849. doi:10.1074/jbc.270.14.7842
47. Wong PT, Choi SK. Mechanisms and implications of dual-acting methotrexate in folate-targeted nanotherapeutic delivery. *Int J Mol Sci*. 2015;16:1772–1790. doi:10.3390/ijms16011772
48. Bolaños K, Macarena S, Albericio F, Kogan MJ, Araya E. Materials Science & Engineering C NIR and glutathione trigger the surface release of methotrexate linked by Diels-Alder adducts to anisotropic gold nanoparticles. *Mater Sci Eng C*. 2021;131:112512. doi:10.1016/j.msec.2021.112512
49. Martín-Sabroso C, Torres-Suárez AI, Alonso-González M, Fernández-Carballido A, Fraguas-Sánchez AI. Active targeted nanoformulations via folate receptors: state of the art and future perspectives. *Pharmaceutics*. 2022;14.
50. Carron PM, Crowley A, O'Shea D, et al. Targeting the Folate Receptor: improving Efficacy in Inorganic Medicinal Chemistry. *Curr Med Chem*. 2018;25:2675–2708. doi:10.2174/0929867325666180209143715
51. Kang C, Han P, Lee JS, Lee D, Kim D. Anchor, spacer, and ligand-modified engineered exosomes for trackable targeted therapy. *Bioconjug Chem*. 2020;31:2541–2552. doi:10.1021/acs.bioconjchem.0c00483
52. Rakshit T, Pal S. Extracellular vesicles for drug delivery and theranostics in vivo. *JACS Au*. 2024;4:318–327. doi:10.1021/jacsau.3c00611
53. Kim HI, Park J, Zhu Y, et al. Recent advances in extracellular vesicles for therapeutic cargo delivery. *Exp Mol Med*. 2024;56:836–849. doi:10.1038/s12276-024-01201-6
54. Koh HB, Kim HJ, Kang SW, Yoo TH. Exosome-based drug delivery: translation from bench to clinic. *Pharmaceutics*. 2023;15:2042. doi:10.3390/pharmaceutics15082042
55. Sharma V, Mukhopadhyay CD. Exosome as drug delivery system: current advancements. *Extracell Vesicle*. 2024;3:100032. doi:10.1016/j.vesic.2023.100032
56. Zhang H, Wang S, Sun M, et al. Exosomes as smart drug delivery vehicles for cancer immunotherapy. *Front Immunol*. 2023;13:1–21. doi:10.3389/fimmu.2022.1093607
57. Jeppesen DK, Fenix AM, Franklin JL, et al. Reassessment of exosome composition. *Cell*. 2019;177:428–445.e18. doi:10.1016/j.cell.2019.02.029
58. Barjesteh T, Mansur S, Bao Y. Inorganic nanoparticle-loaded exosomes for biomedical applications. *Molecules*. 2021;26:1135. doi:10.3390/molecules26041135
59. Kanchanapally R, Deshmukh SK, Chavva SR, et al. Drug-loaded exosomal preparations from different cell types exhibit distinctive loading capability, yield, and antitumor efficacies: a comparative analysis. *Int J Nanomed*. 2019;14:531–541. doi:10.2147/IJN.S191313
60. Sun H, Burrola S, Wu J, Ding WQ. Extracellular vesicles in the development of cancer therapeutics. *Int J Mol Sci*. 2020;21:1–22. doi:10.3390/ijms21176097
61. Man K, Brunet MY, Jones MC, Cox SC. Engineered extracellular vesicles: tailored-made nanomaterials for medical applications. *Nanomaterials*. 2020;10:1–30. doi:10.3390/nano10091838
62. Lara P, Palma-Florez S, Salas-Huenuleo E, et al. Gold nanoparticle based double-labeling of melanoma extracellular vesicles to determine the specificity of uptake by cells and preferential accumulation in small metastatic lung tumors. *J Nanobiotechnology*. 2020;18:1–18. doi:10.1186/s12951-020-0573-0
63. Li G, et al. Facile approach to synthesize gold nanorod @ polyacrylic acid / calcium phosphate yolk – shell nanoparticles for dual-mode imaging and pH / NIR-responsive drug delivery. *Nano-micro Lett*. 2018. doi:10.1007/s40820-017-0155-3
64. Velasco-Aguirre C, Morales-Zavala F, Salas-Huenuleo E, et al. Improving gold nanorod delivery to the central nervous system by conjugation to the shuttle Angiopep-2. *Nanomedicine*. 2017;12:2503–2517. doi:10.2217/nnm-2017-0181
65. Morales-Zavala F, Arriagada H, Hassan N, et al. Peptide multifunctionalized gold nanorods decrease toxicity of β-amyloid peptide in a Caenorhabditis elegans model of Alzheimer's disease. *Nanomed Nanotechnol Biol Med*. 2017;13:2341–2350. doi:10.1016/j.nano.2017.06.013
66. Xu L, Faruqu FN, Liam-or R, et al. Design of experiment (DoE)-driven in vitro and in vivo uptake studies of exosomes for pancreatic cancer delivery enabled by copper-free click chemistry-based labelling. *J Extracell Vesicles*. 2020;9. doi:10.1080/20013078.2020.1779458
67. Bhatta R, Han J, Liu Y, et al. Metabolic tagging of extracellular vesicles and development of enhanced extracellular vesicle based cancer vaccines. *Nat Commun*. 2023;14:1–14. doi:10.1038/s41467-023-43914-8

68. Sancho-Albero M, Navascués N, Mendoza G, et al. Exosome origin determines cell targeting and the transfer of therapeutic nanoparticles towards target cells. *J Nanobiotechnology*. 2019;17:1–13. doi:10.1186/s12951-018-0437-z
69. Ortega A, Martinez-Arroyo O, Forner MJ, Cortes R. Exosomes as drug delivery systems: endogenous nanovehicles for treatment of systemic lupus erythematosus. *Pharmaceutics*. 2021;13:1–28.
70. Choi H, Choi Y, Yim HY, et al. Biodistribution of exosomes and engineering strategies for targeted delivery of therapeutic exosomes. *Tissue Eng Regen Med*. 2021;18:499–511. doi:10.1007/s13770-021-00361-0
71. Huyan T, Du Y, Huang Q, Huang Q, Li Q. Uptake characterization of tumor cell-derived exosomes by natural killer cells. *Iran J Public Health*. 2018;47:803–813.
72. Edelmann MJ, Kima PE. Current Understanding of Extracellular Vesicle Homing/Tropism. *Zoonoses*. 2022;2. doi:10.15212/ZOONOSES-2022-0004
73. He J, Ren W, Wang W, et al. Exosomal targeting and its potential clinical application. *Drug Delivery Trans Res*. 2022;12:2385–2402. doi:10.1007/s13346-021-01087-1
74. Lobos-González L, Aguilar L, Diaz J, et al. E-cadherin determines C aveolin-1 tumor suppression or metastasis enhancing function in melanoma cells. *Pigm Cell Melanoma Res*. 2013;26:555–570. doi:10.1111/pcmr.12085
75. Ganji A, Farahani I, Shojapour M, Ghazavi A, Mosayebi G. In vivo therapeutic effects of colorectal cancer cell-derived exosomes. *IRAN J BASIC MED SCI*. 2020;23:1439–1444. doi:10.22038/ijbms.2020.46465.10730
76. Yang Y, Liu Q, Lu J, et al. Exosomes from plasmodium-infected hosts inhibit tumor angiogenesis in a murine Lewis lung cancer model. *Oncogenesis*. 2017;6:1–12. doi:10.1038/oncsis.2017.52
77. Gharavi AT, Irian S, Niknejad A, Parang K, Salimi M. Harnessing exosomes as a platform for drug delivery in breast cancer: a systematic review for in vivo and in vitro studies. *Mol Ther Oncol*. 2024;32:200800. doi:10.1016/j.omton.2024.200800
78. Fu W, Lei C, Liu S, et al. CAR exosomes derived from effector CAR-T cells have potent antitumour effects and low toxicity. *Nat Commun*. 2019;10. doi:10.1038/s41467-019-12321-3
79. Pavitra E, Dariya B, Srivani G, et al. Engineered nanoparticles for imaging and drug delivery in colorectal cancer. *Semin Cancer Biol*. 2019:1–14. doi:10.1016/j.semcancer.2019.06.017
80. Gaharwar US, Meena R, Rajamani P. Biodistribution, clearance and morphological alterations of intravenously administered iron oxide nanoparticles in male wistar rats. *Int J Nanomed*. 2019;14:9677–9692. doi:10.2147/IJN.S223142
81. Kumar M, Kulkarni P, Liu S, Chemuturi N, Shah DK. Nanoparticle biodistribution coefficients: a quantitative approach for understanding the tissue distribution of nanoparticles. *Adv Drug Deliv Rev*. 2023;194:114708. doi:10.1016/j.addr.2023.114708
82. Tsoi KM, MacParland SA, Ma X-Z, et al. Mechanism of hard-nanomaterial clearance by the liver. *Nat Mater*. 2016;15:1212–1221. doi:10.1038/nmat4718
83. Lara P, Chan AB, Cruz LJ, Quest AFG, Kogan MJ. Exploiting the natural properties of extracellular vesicles in targeted delivery towards specific cells and tissues. *Pharmaceutics*. 2020;12:1–25. doi:10.3390/pharmaceutics12111022
84. Tucci M, Mannavola F, Passarelli A, et al. Exosomes in melanoma: a role in tumor progression, metastasis and impaired immune system activity. *Oncotarget*. 2018;9:20826–20837. doi:10.18632/oncotarget.24846